Stress field estimation from S-wave anisotropy observed in multi-azimuth seismic survey with cabled seafloor seismometers above the Nankai Trough megathrust zone, Japan

T. Kimura[1*], H. Mikada[2], E. Araki[1], S. Kodaira[1], S. Miura[1] and N. Takahashi[3,1]

[1] Research Institute for Marine Geodynamics, Japan Agency for Marine-earth Science and Technology, JPN

[2] Department of Civil and Earth Resources Engineering, Kyoto University, JPN

[3] Network Center for Earthquake, Tsunami and Volcano, National Research Institute for Earth Science and Disaster Resilience, JPN

Corresponding author: *Toshinori Kimura (kimurat@jamstec.go.jp)

Key Points:

- Multi-azimuth seismic surveys around cabled seafloor seismometers were performed above the Nankai Trough megathrust zone, Japan.
- Multi-component dataset and anisotropy semblance method were used to obtain S-wave anisotropy parameter below each seismometer.
- Differential horizontal stress field in the Nankai Trough region was estimated from obtained S-wave anisotropy using a simple crack model.

Abstract

The spatial variation of azimuthal S-wave phase velocity anisotropies caused by differential horizontal stress along the subducting plate at the Nankai Trough was analyzed to understand the stress state of the overhung block of the forearc region, off Kii Peninsula, Japan. We conducted controlled-source seismic surveys along the circumference of a 3 km diameter circle centered at each seismometer of a cabled earthquake observatory installed on the seafloor above the Kumano basin of the Nankai Trough subduction zone. We applied an anisotropy semblance method to estimate the orientation of fast and slow S-wave velocities of both shallow sediments and deep accretionary prism using the multi-azimuth seismic dataset acquired at each seismometer location. The estimated orientations of fast S-wave velocity are parallel to the convergent direction of the subducting place beneath the Kumano basin in the deeper accretionary prism while perpendicular to the convergent direction in the shallow sediments inside the Kumano basin. The orientations of these fast S-wave polarization show good agreement with those of horizontal maximum stress orientations estimated in situ borehole measurements in the observation area Then differential horizontal stress field in the Nankai Trough region was estimated from obtained S-wave anisotropy using a simple crack model. The azimuths of fast S-wave polarization and the derived differential stresses could be explained well by the tectonics of the Nankai Trough subduction zone. These results strongly suggested that the S-wave azimuthal anisotropy measurements could be used to monitor the subsurface stress field as a function of time.

1 Introduction

The Nankai Trough, Japan, is a major subduction zone formed by the subducting Philippine-sea plate beneath the Eurasian plate with a rate of approximately 4-6.5 cm/year, and over M 8.0 massive megathrust earthquake occurred along the plate interface repeatedly with intervals of 100 to 150 years [*Ando*, 1975; *Seno*, 1993; *Miyazaki and Heki*, 2001; *Kodaira et al.*, 2006]. These earthquakes generate strong ground motion and huge tsunamis, which cause severe and widespread damage in the coastal urban area in the south-central part of Japan. The 1944 Tonankai earthquake and 1946 Nankai earthquake are the last megathrust earthquakes that occurred along the Nankai Trough [e.g., *Kanamori*, 1972]. Consequently, more than 70 years have passed since the last earthquakes, and the next earthquake is anticipated to take place in the near future. Because of the hazardous nature of large-scale earthquakes in the Nankai Trough subduction zone, it is essential to understand the processes that govern the distribution, the mechanism, and the style of the slip motion along the plate boundary for earthquake and tsunami hazard assessment. Recent studies have provided new insights into the interplate earthquakes in the Nankai Trough. *Wallace et al.* [2016] analyzed an Mw 6.0 earthquake and associated aftershocks with respect to the geodetic deformation of the seafloor using both tidal pressure gauges and borehole pore pressure sensors and found out the evidence for a few-days' long afterslip soon after the mainshock. *Araki et al.* [2017] reported that slow slip events (SSEs) repeatedly occur every 8 to 15 months and that the SSEs play a vital role in releasing accumulated strain along the seismogenic interplate region to accommodate 30 to 55 % of the plate motion. *Suzuki et al.* [2016] suggested that SSE occurred in the shallow part of the sedimentary wedge triggered in the regional stress accumulation and release processes along the Nankai trough and concluded that the continuous and careful monitoring of crustal activities

provides an effective way to detect preseismic signals of large earthquakes. *Lin et al.* [2015] investigated the stress states of both the Japan Trench and the Nankai Trough subduction zones. They hypothesized that the Nankai Trough is still in an early stage of the stress accumulation towards the next great earthquake if the stress state changes from the compression to the extension after a megathrust earthquake, as observed before and after the 2011 earthquake off the Pacific coast of Tōhoku. These studies indicate that the stress state at the subduction zones would be the key to understand the occurrences of the megathrust earthquakes. The stress state as a function of time towards the next megathrust earthquake in the Nankai Trough subduction zone would be indispensable to understand the preparation and the generation cycle of subduction earthquakes.

Some conventional techniques observe in situ stress in subduction zones, including borehole strainmeter, borehole breakout analysis, and anelastic strain recovery (ASR) measurements using core sample [e.g., *Lin et al.*, 2015]. These techniques can provide in situ stress properties, especially for horizontal stress, around the boreholes. As *Wallace et al*. [2016] and *Araki et al*. [2017] have reported, borehole interstitial fluid pressure sensors could be used to constrain the stress state in the sediments above subduction zones. Seafloor pressure gauges could be exploited to estimate stress accumulation at the plate interface [*Suzuki et al.*, 2016]. Borehole strainmeters or interstitial fluid pressure sensors providing exciting data need to be installed in drilled boreholes. ASR measurement is a method for effectively estimating three-dimensional in situ stresses of core samples extracted from drilled holes. Seafloor pressure gauges are installed to detect tidal changes and tsunamis as part of earthquake monitoring systems in which the number of sensors is in general limited. Therefore, it is worth looking to use seismic sensors to monitor stress state in subduction zones. We would like to propose a method to utilize seismic sensors to complement more number of time-variant quantitative data to understand the developing stress state of the Nankai Trough subduction zone. The method we propose uses S-wave anisotropy as a proxy of the stress field to estimate the wide-area distribution of the horizontal stress field in the subduction zone. S-wave anisotropy is mainly affected by cracks induced by the differential horizontal stress in the rock [e.g., *Crampin*, 1981; *Gao and Crampin*, 2004], and therefore, stress field estimation along the subduction zone becomes possible by S-wave anisotropy analysis using multi-component seismic data. Several results were obtained from S-wave anisotropy analysis for seismic survey data in the Nankai Trough subduction zone. *Tsuji et al*. [2011a] showed S-wave anisotropy's spatial distribution using P-S converted waves generated by an airgun array source acquired with a tri-component ocean bottom seismometers (OBS'es) arranged along a two-dimensional survey line in the Kumano basin. *Tsuji et al.* [2011b] also observed S-wave anisotropy in a VSP (Vertical Seismic Profile) survey conducted in a borehole and estimated the orientations of principal horizontal stress for a depth zone of 150 m thickness, including gas-rich layers below the basin. These results revealed a complex distribution of horizontal maximum stress orientation, but no depth variation has been investigated. As *Haacke et al.* [2009] introduced, a layer-stripping method estimates depth-dependent S-wave anisotropy in marine OBS survey with multi-azimuth shooting, depth-dependent S-wave anisotropy, i.e., the orientation of horizontal maximum stress could be driven. There are only a few examples of depth-dependent S-wave anisotropy analysis below the seafloor. Moreover, as introduced by *Okamoto et al*. [2013], a method stress analysis could be introduced to provide the quantitative horizontal differential stresses as well as the orientation of horizontal maximum stress.

In this study, we acquired seismic data by the seismometers, most of which were deployed in a cabled observatory named DONET (Dense Oceanfloor Network System for Earthquake and Tsunamis) [*Kawaguchi et al.*, 2015] and the others in the IODP borehole observatories [*Kopf et al.*, 2010; *Kimura et al.*, 2013] in and around the Kumano basin. DONET seismometers are deployed on the seafloor, while the borehole observatories both on the seafloor and in the boreholes. We conducted circular airgun shootings around each seismometer location with a ca. 3 kilometers diameter to estimate azimuthal differences in the S-wave propagation caused by the anisotropic phase velocities and their spatial distribution. In analyzing azimuthal S-wave anisotropy, we proposed a new scheme to use an anisotropic semblance method to estimate both the fast S-wave's azimuth polarization and the quantitative difference between the fast and slow S-wave phase velocities. A layer stripping algorithm is then applied to obtain depth-dependent S-wave anisotropy in the deep accretionary prism zone. Both shallow and deep S-wave anisotropies are used as a proxy of the stress field below every seismometer. We introduced a wing crack model to estimate differential horizontal stress quantitatively for obtained S-wave anisotropy. Comparing our results with the estimated differential stresses showed good agreement with those by the other methods such as an anelastic strain recovery (ASR) method or borehole breakout analyses. Our results imply that the seismic anisotropy analysis could be used as a tool to estimate stress orientation and the quantitative value of horizontal differential stress as a function of depth below each seismometer location. We think that circular airgun shooting surveys in a time-lapse manner could be used to monitor the stress accumulation process of overhung to discuss the wide-area distribution of differential horizontal stress in the Nankai Trough subduction zone.

2 Method and synthetic test

In a medium under horizontal stresses of orientation dependency, S-wave velocities become a function of azimuth. The stiffness matrix in the theory of elasticity to describe such medium has 5 independent elements in the first-order approximation, and the medium is called a transverse isotropic medium with a horizontal axis of symmetry (HTI). S-waves traveling vertically through a horizontally stratified HTI medium would be split into fast and slow S-waves [*Crampin*, 1981]. Because of changes to the fluid-saturated stress-aligned grain-boundary cracks and pore throats pervading almost all in situ rocks in the crust down to the upper mantle, the polarizations of the faster split S-waves have been observed approximately parallel to the orientation of maximum horizontal stress [*Crampin and Chastin*, 2003]. S-waves propagating from artificial sources at multi-azimuth locations to a sensor could be exploited to estimate the orientation and the magnitude of differential stress from acquired seismic data. Although explosive source generates only P-waves in water, P-S converted up-going waves generated at boundaries of elastic properties in the formations below the seafloor would be recorded in radial and transverse components at every seismometer. Therefore, multi azimuth shootings with a constant offset from every shot location to the seismometer could provide azimuthal coverage for acquiring azimuthal anisotropy of S-wave velocities. S-wave splitting in HTI media results from propagation through stress-aligned fluid-saturated grain-boundary cracks and pore throats [*Crampin and Chastin*, 2003], and, therefore, S-wave splitting analysis would allow us to estimate stress field including orientation and amplitude if the cracks are stress-aligned ones. Figure 1 depicts a top view of the survey image, describing the relationship between horizontal stress and aligned cracks. We use "anisotropy semblance" to obtain depth-dependent S-wave anisotropy parameters, including the azimuths of the fast S-wave polarization and the time delay

between fast (S1) and slow (S2) S-wave, below seismic observatory from multi azimuth controlled-source survey data [*Kimura et al.*, 2016]. Multi azimuth radial and transverse components in the anisotropic medium can be written as equations (1)-(4) [*Bale et al.*, 2013].

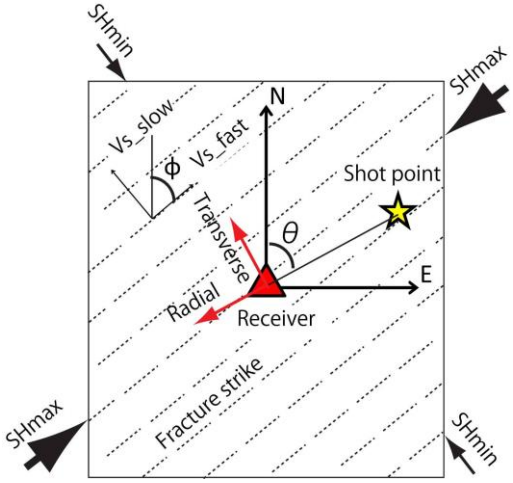

Figure 1. Schematic drawing of the multi-azimuth survey in a stress-induced anisotropic medium. The azimuth of the fast S-wave polarization is generally coincident with the orientation of principal horizontal stress.

$$R(t,\theta) = \bar{A}(t) + \Delta A(t)\cos[2(\theta-\phi)], \quad (1)$$

$$T(t,\theta) = \Delta A(t)\sin[2(\theta-\phi)], \quad (2)$$

$$\bar{A}(t) = \frac{1}{2}[A(t) + A(t-\tau)], \quad (3)$$

and

$$\Delta A(t) = \frac{1}{2}[A(t) - A(t-\tau)], \quad (4)$$

where ϕ represents the azimuth of fast S-wave polarization and θ represents that of the shot from the receiver. *A(t)* represents the shot response obtained by the convolution between source function and reflection coefficients. τ is the time delay between S1 and S2. In this study, we obtain ϕ and τ by using anisotropy semblance. The anisotropy semblance is defined by equations (5)-(6),

$$S(\tau,\phi) = \max\left(\sum_{\theta=0}^{2\pi} R(t+\tau'(\theta),\theta)\right), \quad (5)$$

$$\tau'(\theta) = \begin{cases} 0 & (\phi - \Psi < \theta < \phi + \psi) \\ \tau & (\phi + \pi/2 - \Psi < \theta < \phi + \pi/2 + \psi) \\ 0 & (\phi + \pi - \Psi < \theta < \phi + \pi + \psi) \\ \tau & (\phi + 3/2\pi - \Psi < \theta < \phi + 3/2\pi + \psi) \\ 0 & (Otherwise) \end{cases}, \quad (6)$$

where S(τ, ϕ) represents the anisotropy semblance as a function of τ and ϕ. ψ represents the width of the rectangular function defined by equation (6). We built a 1-D layered model to see how the time delay influences the arrival time variation in the circular shooting using Equation (1). The 1-D model has 2000 m thickness with 2000 m/s and 1000 m/s for P- and S-wave velocities, respectively. We fixed the azimuth of the fast S-wave polarization (ϕ = 30 degrees in Figure 1) and changed τ from 20–160 ms corresponding to 1.0–7.5 % of the difference in the slow S-wave velocity from the given S-wave velocity in the first layer of the 1-D model. Figure 2 shows the variation of the arrival times of the wave's radial component against the azimuth of the shot location (θ in Figure 1). When time delay τ is smaller than or equal to 40 ms, the apparent arrival time of the radial component of a wave varies as a sinusoidal curve of the amplitude τ in the time axis against the azimuth angle. As τ increases, the sinusoidal curve for small τ, however, asymptotically approaches to a rectangular function with the amplitude of τ against the azimuth of the shot location. For dealing with both the sinusoidal and rectangular shapes in the arrival times to calculate the semblance S(τ, ϕ) no matter what the value of τ would be, Equation (6) needs to be applied to both small and large τ with appropriate values of ψ. We finally found that the value S(τ, ϕ) is to be optimized at the maximum value for ψ = 30 degrees.

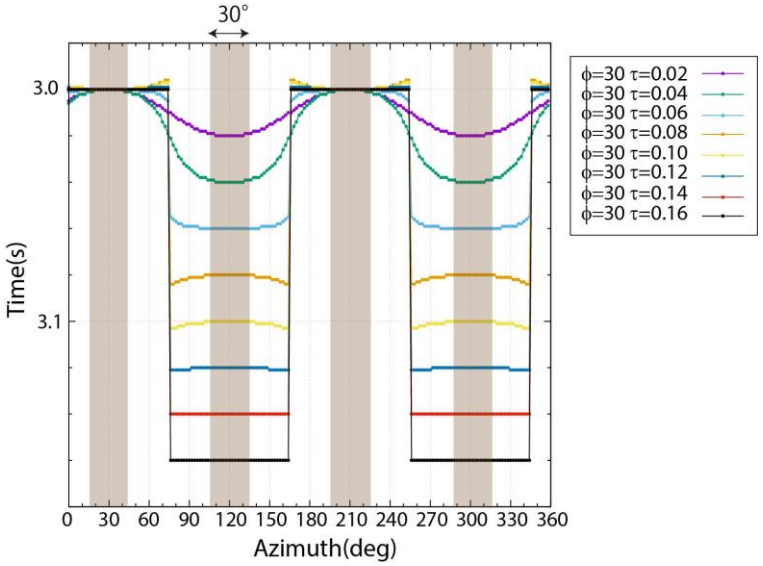

Figure 2. Variations of the peak amplitude of radial synthetic records calculated from simple 1-D layered models. In a strong anisotropy model, the peak amplitude takes a rectangle shape from an apparent sinusoidal shape calculated from weak anisotropy models.

We performed a 3-D numerical simulation using the finite difference method for a medium causing S-wave splitting [*Bansal and Sen*, 2008] to justify the applicability of our new method. Figure 3 shows that our 3D simulation model consists of three layers, i.e., seawater, shallow sediment, and accretionary prism layers. A receiver is placed on the seafloor, and an impulsive compressional source signal was generated along a circle of a 3 km radius centered at the receiver location for every 10 degrees. We added the fluctuation to the circle radius, which follows the Gaussian distribution with the maximum value of ±30 m error, which may routinely be observed in field surveys.

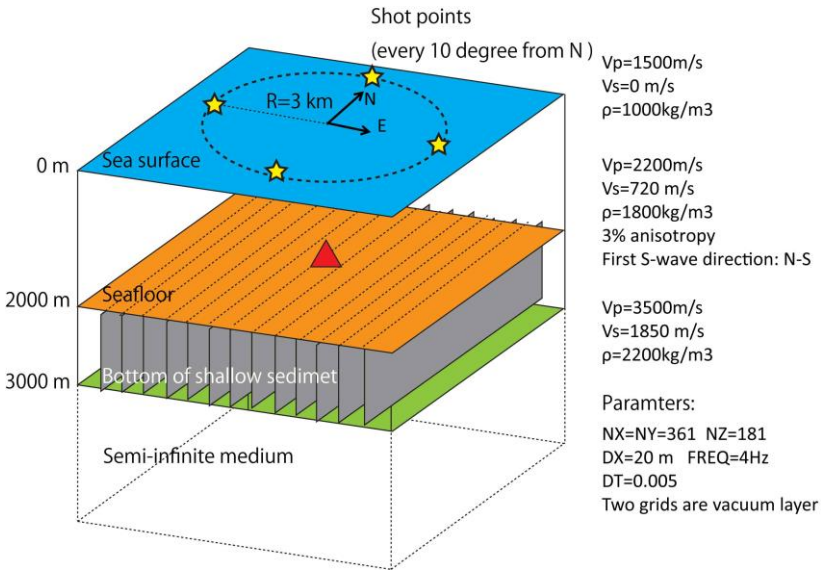

Figure 3. A simple layered model used for the synthetic test. An isotropic medium is located at the shallow sediment layer, which has 3 % anisotropy with the azimuth of the fast S-wave polarization is north-south.

a) Synthetic records computed from the 3-D anisotropy model

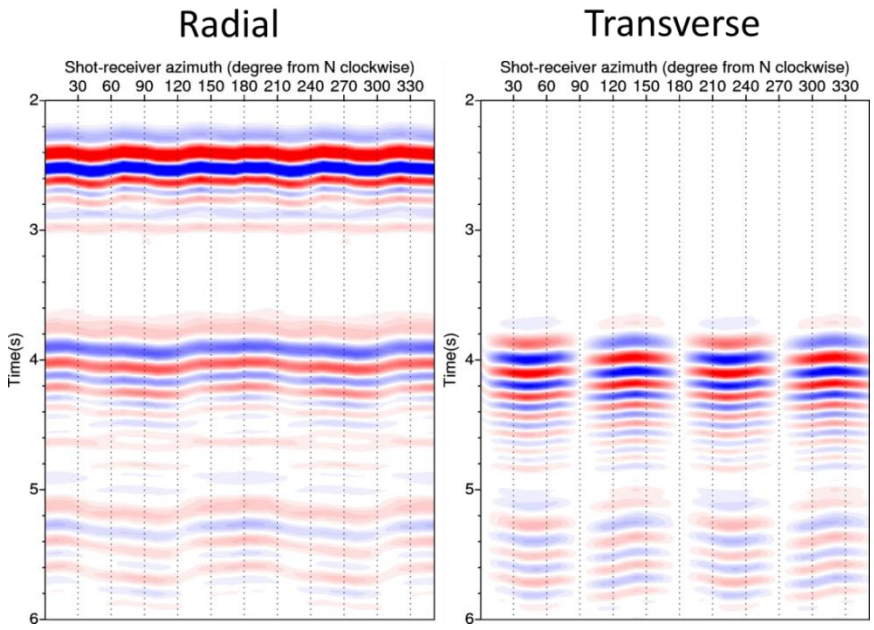

b) Obtained anisotropy parameters calculated from the synthetic records.

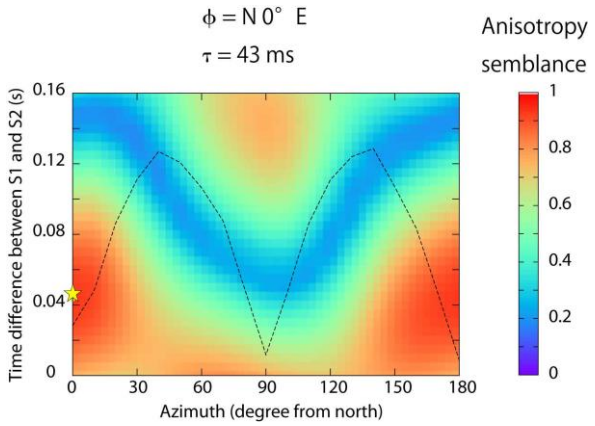

Figure 4. a) Synthetic radial and transverse records computed from the 3-D velocity model shown in Figure 3. b) Obtained S-wave anisotropy parameters calculated from the synthetic records.

We introduced the anisotropy semblance method to the simulated synthetic records. We first applied the technique to raw synthetic records for the model giving τ and ϕ 43 ms and 0 degrees, respectively. Estimated τ and ϕ are 48 ms and 10 degrees, respectively, due to the fluctuation in the radius of the circle of source locations, which produces about 30 ms error in the travel time. We then applied a moving average method to acquired waveforms for every shot point along the circle for both radial and transverse for the range of 30 degrees. After applying the same anisotropy semblance method, we could obtain τ=43ms and ϕ=0, respectively, showing

3% of anisotropic S-wave phase velocity difference and 0 degrees in the azimuth of the fast S-wave polarization in the shallow sediments (Figure 4). Obtained anisotropy parameters are completely coincident with the values given to the synthetic model.

3 Data acquisition

We conducted a series of active seismic surveys, KR13-17, KR15-05, KR15-08, and KR16-11 conducted by R/V Kairei, in the Nankai Trough area to estimate spatially varying S-wave anisotropy, which would reflect the difference in the stress state of subseafloor materials along the subduction zone since 2013 to 2016 [*JAMSTEC*, 2014; *JAMSTEC*, 2015a; *JAMSTEC*, 2015b, *JAMSTEC*, 2016]. A tuned airgun array system of 7800 cubic inches was deployed as a seismic source that was fired along the circular lines, shown in Figure 5, each of which encloses a seafloor seismometer of the DONET cabled observatory, a borehole seismometer installed during the legs of the IODP (Integrated Ocean Drilling Program), or both (Table 1). The seismometers of DONET are all telemetered in realtime for the observation of natural earthquake events such as regional microearthquakes, VLF (Very Low Frequency) events, and seismic microtremors in and around the seismogenic zone [*NIED*, 2019]. The seismometers of the IODP borehole observatory are also telemetered in realtime by using DONET cable [*IMG FEAT/JAMSTEC*, 2016]. Therefore, it was possible to check the data quality in realtime when acquiring seismic signals generated by the airgun system. Furthermore, the DONET seismometers were buried in the seafloor with a depth of 1 m for improving the coupling of the seismometers to subseafloor formation. The quality of horizontal components of acquired waveforms becomes relatively higher than the acquired by conventional ocean bottom seismometer without burial.

For each circular shooting line in Figure 5, the first shot was fired at the location right north to the center of the circle, i.e., every seismometer location, and the shots following the first one were successively fired along the survey line of ca. 3km radius circle at every 2.0 degrees in the azimuth. The seismometers of the DONET and borehole observatory acquire seismic data with the sampling rates of 5 and 8 ms, respectively. We tried to hold the vessel's route to draw a circle of 3 km radius centered at each of the seismometers and could keep the deviation from the circle within ±30 m for almost all the shooting lines. The same circle was traced to fire the airgun system from time to time to confirm both the stability and the repeatability of the S-wave anisotropy survey. After the data acquisition, we first extracted the shot records from the continuous output from the seismometers to produce both the radial and the transverse components to the shot location from the two horizontal components by using the orientation of DONET seismometers given by *Nakano and Tonegawa* [2012]. Figure 6 shows an example of observed data of the KMB07-R3 survey line during the KR13-17 cruise.

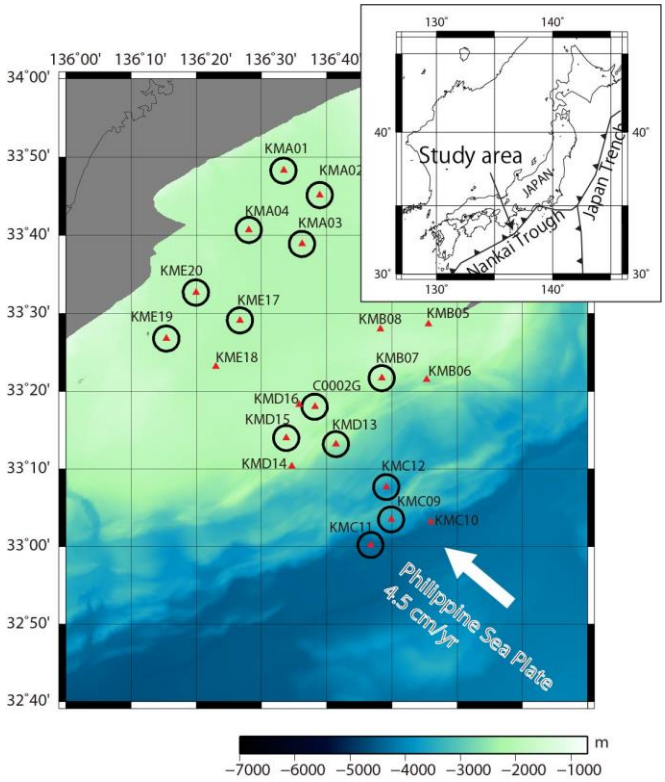

Figure 5. Location map of seafloor and borehole observatories with airgun shooting lines. Triangles show locations of observatories. Circles indicate airgun shooting lines around observatories with a 3 km radius.

Table 1. List of circular shooting lines conducted during each cruise.

Line name	Offset (km)	KR13-17	KR15-05	KR15-08	KR16-11	Total
KMA01-R3	3				1	1
KMA02-R3	3			1		1
KMA03-R3	3			1		1
KMA04-R3	3	1	1		3	5
KMB07-R3	3	1	1			2
KMC09-R3	3	2	1		1	4
KMC11-R3	3			1		1
KMC12-R3	3	2	1		1	4
KMD13-R3	3	2	1		1	4
KMD15-R3	3	1	1		1	3
KME17-R3	3	1	1	12		14
KME19-R3	3			1		1
KME20-R3	3			1		1
C0002G-R3	3	2	4	3	2	11

Total	12	11	20	10	53

Cruise periods:
KR13-17: November 7-15, 2013
KR15-05: March 21-31, 2015
KR15-08: June 11-8, 2015
KR16-11: September 15-22, 2016

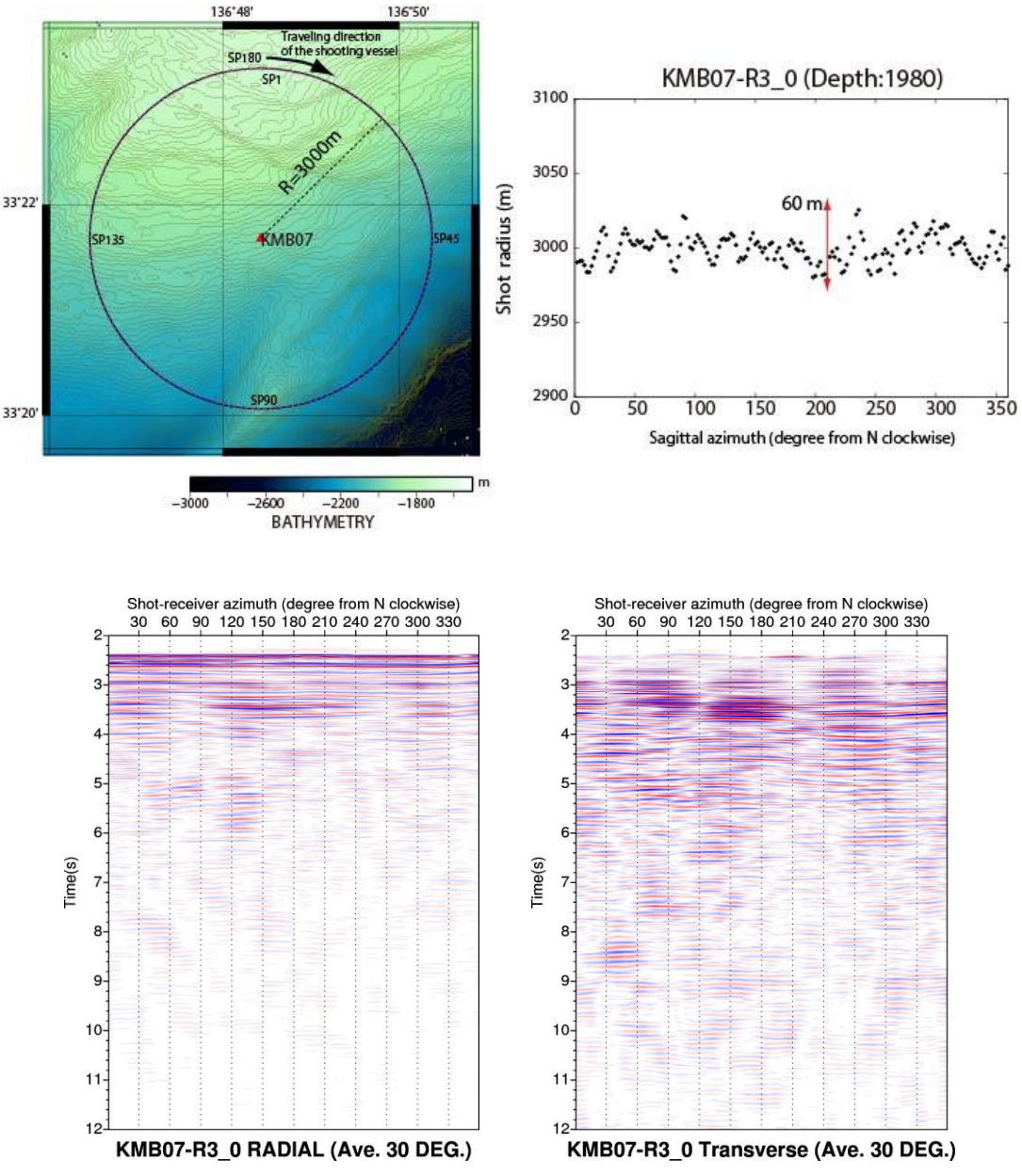

Figure 6. Example of shooting points and observed horizontal records of KR13-17 cruise. (a) KMB07-R3 circle shooting line. The shooting radius from the observatory was kept within ±30

m from the target radius (3km). (b) Observed data, radial, and transverse records of the KMB07-R3 line with binning in range of 30 degrees.

Clear events of high amplitudes spanning the four-quadrant angles in the azimuth are visible in both radial and transverse records between 2.0 to 4.0 s. Since simple 2-D numerical simulation for the model shown in Figure 3 confirms that the events would be the P-S converted waves reflected at the bottom of shallow sediment layers with a depth of 1 km as shown in Figure 7, the events might be P-S converted waves propagating shallow sediment layers. The other reflection event such as P-S converted waves reflected at the top of oceanic crust, i.e., the plate boundary is also visible around 7.4 s for the offset of 3000 m as shown in the common receiver gather in Figure 7 following the structure estimated by *Kamei et al*. [2012]. However, it is difficult to identify the reflection events in the field data due to the weak amplitude and the superposition of the other events, such as water reverberations and peg-legs generated by both the seafloor and shallow sediment layer. Therefore, it is necessary to apply a data processing technique to retrieve weak converted signals from the observed data to discuss S-wave anisotropy in the deep.

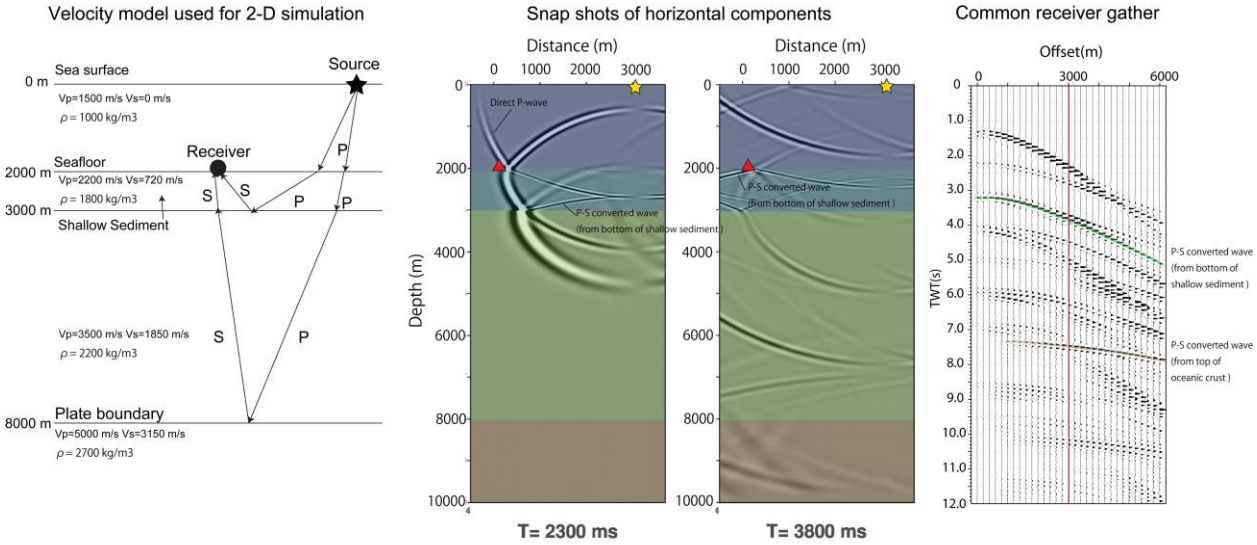

Figure 7. A velocity model used for 2-D seismic wave propagation simulation, a snapshot of the horizontal receiver, and a common receiver gather. P- and S-wave velocities in each layer are given with reference to *Kamei et al.* [2012] and estimated using Castagna's equation [*Castagna et al.*, 1985] the empirical relation between P- and S-wave velocities in wet sediments.

4 Data processing and results

4.1 Anisotropy Estimation

We applied the method of anisotropy semblance to estimate the azimuth of the fast S-wave polarization ϕ and the time delay τ that maximizes the value of $S(\tau, \phi)$ in Equation (5)

using the multi-azimuth seismic data observed by DONET and borehole seismometers. In this analysis, we assumed a horizontally stratified three-layer model, comprised of shallow sediment, accretionary prism, and oceanic crust layers, for each seismometer as the sub-seafloor structure with reference to a 2D velocity structure [*Kamei et al.*, 2012], with which the structure matches in the orthogonal projection. We applied the Alford rotation [*Alford*, 1986] and a layer stripping algorithm [*Thomsen et al.*, 1999] to the radial and transverse data to estimate depth-depended azimuth of the fast S-wave orientation and the time difference between the fast and the slow S-wave arrivals from the observed horizontal components of seismic data. In the analysis, seismic records showing clear P-S converted waves are used to avoid any influence of 3D subseafloor topography. We used seismic events between 3.0 to 5.0 s as converted P-S wave from the bottom of shallow sediment and 6.0 to 8.0 s as converted P-S wave from the top of the oceanic crust. Figure 8 depicts radial and transverse records observed by the KMD15 seismometer and obtained anisotropy parameters by anisotropy semblance method. Solid lines indicate RMS amplitudes of the transverse component, and the azimuth of the fast S-wave polarization and the time delay between fast and slow S-wave are indicated as stars in Figure 8.

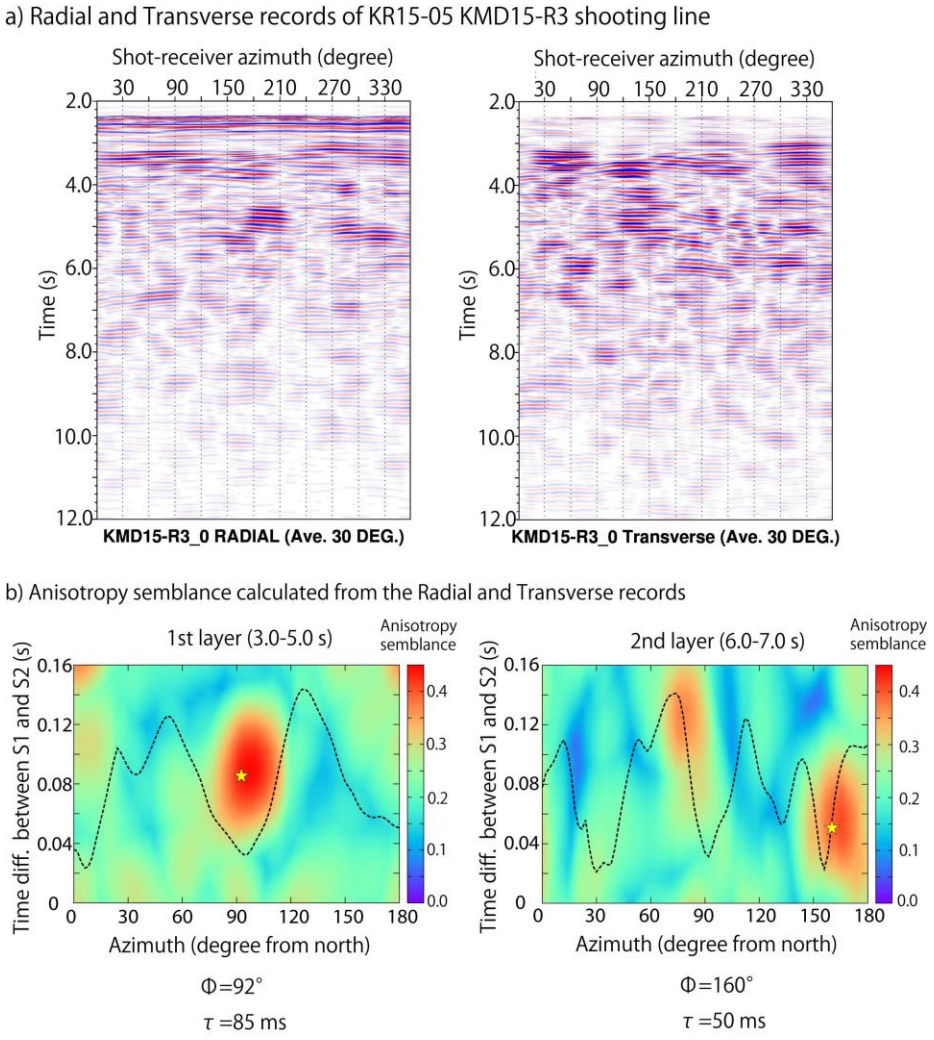

Figure 8. a) Radial and transverse components observed by KMD15 seismometer with multi-azimuth airgun shootings. b) Results of anisotropy semblance methods of KMD15 seismometers in the 1st layer (left) and the 2nd layer (right). The vertical axis shows the time delay, and the horizontal azimuth indicates the azimuth of the fast S-wave polarization. Color contour shows the value of anisotropy semblance. Stars indicate the optimum values of the time delay and the azimuth of the fast S-wave polarization. Black dashed lines show the RMS amplitude of transverse components.

4.2 Differential Stress Estimation

After estimating both the azimuth of the fast S-wave polarization and the time difference between the fast and slow S-wave arrivals, we simply treat them as the horizontal maximum stress orientation and the magnitude of horizontal differential stress, respectively. We consider a random crack model under azimuthally different stress loading for quantitative conversion from the time difference between the fast and the slow S-wave arrivals. Fig. 9 depicts three schematic images of the crack model with horizontal differential stress loading.

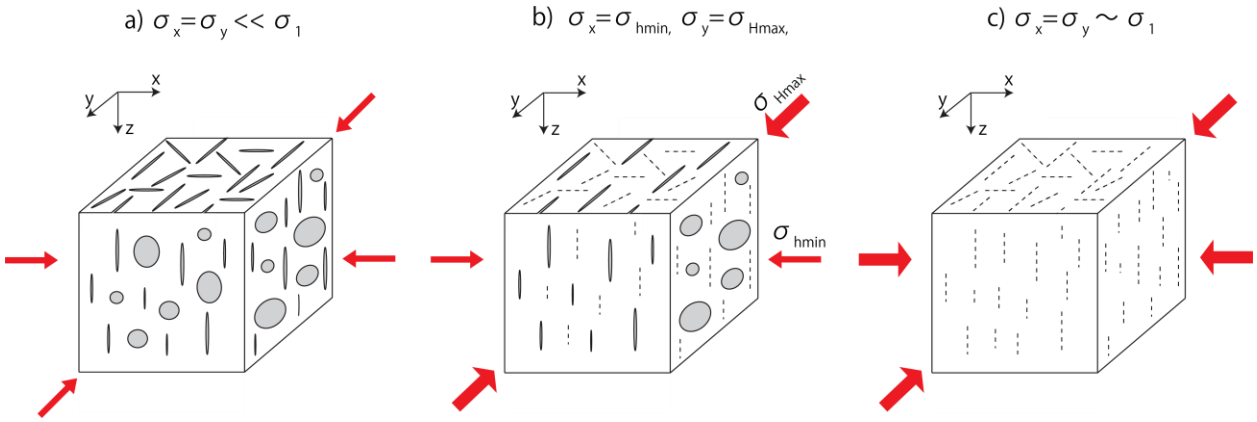

Figure 9. Schematic images depicting the relationship between differential horizontal stress and cracks. a) Horizontal stresses are equivalent and much smaller than principal stress. b) σ_x and σ_y are minimum and maximum horizontal stresses, respectively. c) Horizontal stresses are equivalent and close to maximum principal stress.

For further discussion, the following assumptions have been made: 1) both the shallow sediments and accretionary prism are of HTI (Transversally Isotropic with the Horizontal axis of symmetry) media, in which the orientation of microcracks are aligned to that of horizontal maximum stress, 2) microcracks in the media have a constant aspect ratio, and 3) all microcracks except cracks aligned with the orientation of horizontal maximum stress are closed due to a stress normal to the crack plane when the magnitude of the stress becomes greater than or equal to that of the horizontal minimum stress. We use the following equations given by *Nur* [1971] to

discuss the relationship between the amplitude of S-wave anisotropy and differential horizontal stresses.

$$\alpha \leq \frac{\sigma_n}{E_0} \qquad (7)$$

where α represents an aspect ratio of a microcrack, σ_n and E_0 a stress and the Young's modulus normal to the microcrack plane. If the condition in Equation (7) is satisfied, the microcrack is closed. We assume that σ_{Hmax} and σ_{hmin}, i.e., horizontal maximum and minimum stresses, respectively, are parallel to the azimuths of the fast and the slow S-wave polarizations. Therefore, the Young's moduli, E_1 and E_2 are chosen to the orientations of the fast and the slow S-wave polarization, respectively. Two cracks with the same aspect ratio aligned in the azimuths orthogonal to each other would satisfy the following conditions [*Okamoto et al.*, 2013].

$$\alpha \leq \frac{\sigma_{Hmax}}{E_1} \qquad (8)$$

$$\alpha > \frac{\sigma_{hmin}}{E_2} \qquad (9)$$

Therefore, the minimum value for the horizontal maximum stress and the maximum value of the horizontal minimum stress could be expressed as follows.

$$\min\left(\sigma_{Hmax}\right) = \alpha E_1 \qquad (10)$$

$$\max \ \ \sigma_{hmin} \ < \cong \alpha E_2 \qquad 11$$

The following equation gives the minimum differential value between the horizontal maximum stress and the horizontal minimum principal stress.

$$min(\Delta\sigma_H) = min(\sigma_{Hmax} - \sigma_{hmin}) \qquad (12)$$

Finally, the following equation would give a relationship between the minimum differential stress, aspect ratio of crack, and the Young's modulus.

389 $$min(\Delta\sigma_H) > \alpha\Delta E \qquad (13)$$

390

391 ΔE represents a differential value between the Young's modulus of E_1 and E_2, which can be
392 calculated using the following equations.

393

394 $$E_1 = \rho {V_{s_1}}^2 \frac{3{V_{p_1}}^2 - 4{V_{s_1}}^2}{{V_{p_1}}^2 - {V_{s_1}}^2} \qquad (14)$$

395 $$E_2 = \rho {V_{s_2}}^2 \frac{3{V_{p_2}}^2 - 4{V_{s_2}}^2}{{V_{p_2}}^2 - {V_{s_2}}^2} \qquad (15)$$

396

397 Where ρ represents the density, V_{p1}, V_{p2} respectively represent the fast and slow P-wave
398 velocities. V_{s1}, V_{s2} respectively represent the fast and slow S-wave velocities. We will discuss
399 the relationship between S-wave anisotropy parameters and differential horizontal stress using
400 the equations (7)-(15). Although the influence of P-wave anisotropy is relatively small, we
401 assume the same magnitude of anisotropy to be applied to both P- and S-waves in the following
402 discussion.

403 It is known that the aspect ratio of crack can be changed by the effective confining
404 pressure in the rock sample [*Schubnel et al.*, 2006]. Following the discussion of Schubnel et al.
405 [2006], we assume the aspect ratios for the shallow sediments and the accretionary prism to be
406 0.005 and 0.003, respectively, to estimate the minimum horizontal differential stresses using the
407 cross-plots shown in Figure 10.

408 The results of our analysis, i.e., the arrivals of the fast S-waves, the azimuths of the fast
409 S-wave polarization, the time delays of the slow S-wave arrival, and the estimated minimum
410 differential stresses, for each seismometer for both shallow sediments and deep accretionary
411 prism are summarized in Table 2 as well as the assumed S-wave velocity and the thickness of the
412 layer. Obtained results suggest that differential horizontal stress in the shallow sediments is
413 generally smaller than those in the accretionary prism. Figure 11 shows obtained the azimuth of
414 the fast S-wave polarization and amplitude of S-wave anisotropy. Results show variations
415 obtained from repeated shootings conducted in different yearly cruises and/or on the same
416 cruises. Figure 12 depicts the spatial distribution of horizontal differential stress in the shallow
417 sediment and the accretionary prism layers. Averaged values are used in the observatories, where
418 repeated surveys were conducted.

419

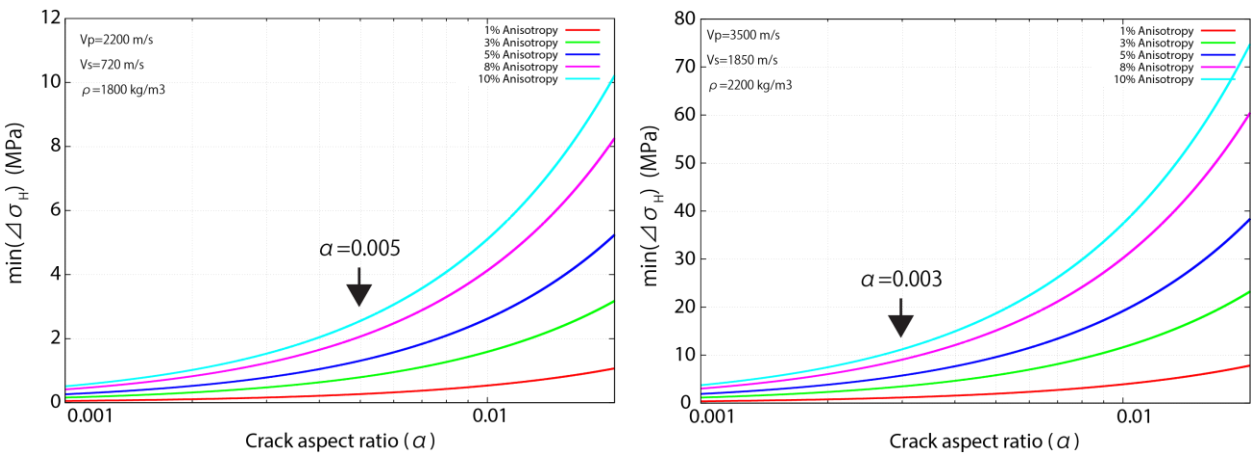

Figure 10. (Left) The relationship between the aspect ratio of crack and the minimum value of horizontal differential stress in the shallow sediment layer. (Right) The relationship between the aspect ratio of crack and the minimum value of horizontal differential stress in the accretionary prism layer. Both relationships are calculated by using equation (11), (12), and (13) with the velocity model.

Table 2. 1-D velocity models used for the anisotropy semblance method and obtained results, including azimuths of fast S-wave velocity and amplitude of anisotropy for each site and layer. a) model and results for shallow sediment layer. b) model and results for accretionary prism.

a) 1st layer (shallow sediment)

Site ID	Event time (sec)	Azimuth (degree)	Time delay (msec)	S-wave velocity (m/s)	Thickness (m)	Anisotropy (%)	Horizontal differential stress (Min. MPa)
KMA02	3.5	42	20	720	1200	1.2	0.3
KMA02	4.0	40	20	720	1200	1.2	0.3
KMA03	3.5	134	10	720	1200	0.6	0.2
KMA04	4.0	176 - 182	70	720	1200	4.0	1.1
KMB07	3.2	24 - 30	50 - 65	720	1000	3.5 - 4.5	0.9-1.2
KMC09	-	-	-	-	-	-	-
KMC12	3.9	122	60	720	1200	3.5	0.9
KMD13	4.0	144 - 148	60 - 65	720	1200	3.5 - 3.8	0.9-1.0
KMD15	4.0	90 - 94	85	720	1200	4.9	1.2
KME17	3.5	26 - 32	5 - 10	720	1000	0.4 - 0.7	0.1-0.2
KME19	3.5	36	45	720	1000	3.1	0.8
KME20	3.5	24	25	720	1000	1.8	0.5
C0002G	3.5	60	80	720	1000	5.4	1.5

b) 2nd layer (accretionary prism)

Site ID	Event time (sec)	Azimuth (degree)	Time delay (msec)	S-wave velocity (m/s)	Thickness (m)	Anisotropy (%)	Horizontal differential stress (Min. MPa)
KMA01	7.0	122	15	1850	4000	0.9	1.0
KMA02	5.5	98	15	1850	3000	0.9	1.0
KMA03	7.0	110	5	1850	4000	0.2	0.2
KMA04	6.5	108 - 112	50 - 65	1850	3500	2.6 - 3.3	2.7-3.5
KMB07	7.0	146 - 152	135 - 145	1850	4000	5.9 - 6.3	6.1-6.5
KMC09	5.5	116 - 126	115 - 120	1850	4000	5.1 - 5.3	5.3-5.5
KMC12	7.0	133	55	1850	3000	3.3	3.4
KMD13	6.0	142 - 144	80 - 85	1850	3000	4.7 - 5.0	4.9-5.2
KMD15	6.5	154 - 160	45 - 50	1850	3000	2.7 - 3.0	2.8-3.1
KME17	7.0	114 - 122	40 - 55	1850	5000	1.5 - 2.0	1.6-2.1
KME19	7.5	160	110	1850	5000	3.9	4.1
KME20	7.5	120	50	1850	5000	1.8	1.9
C0002G	7.5	144	40	1850	4000		1.9

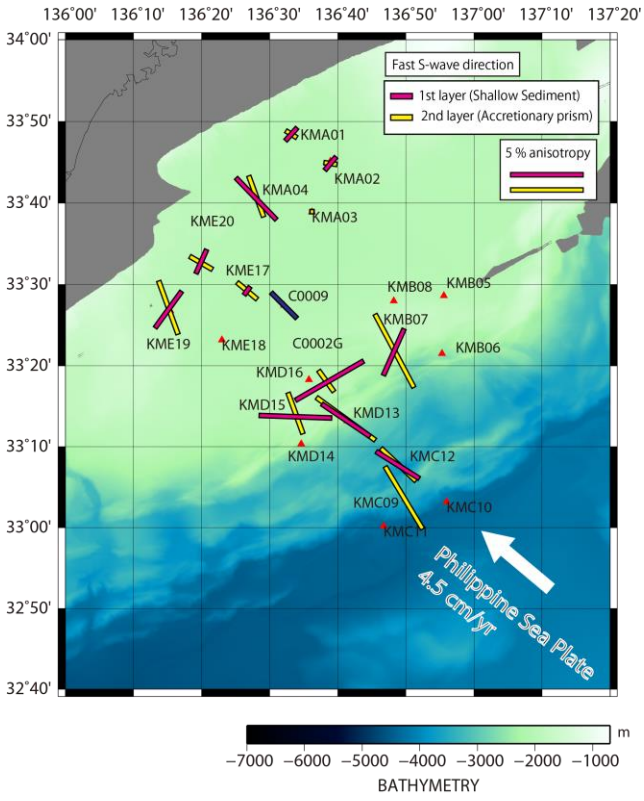

Figure 11. Wide area distribution of the azimuth of the fast S-wave polarization obtained from the anisotropy semblance analysis. Magenta and yellow bars indicate the azimuth of the fast S-wave polarization in shallow sediment and accretionary prism, respectively. The blue bar indicates the orientation of principal horizontal stress obtained by borehole breakout analysis (135°±11° at a depth of 1300-1550m below seafloor) in the IODP C0009 borehole [*Lin et al.*, 2010].

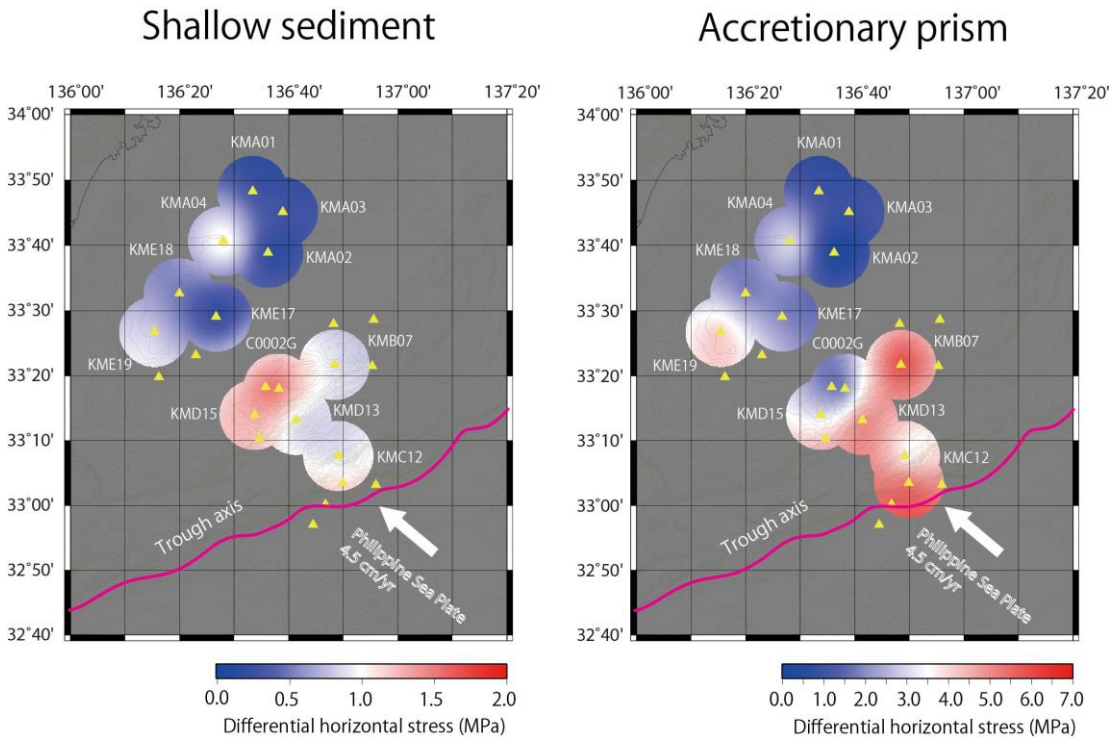

Figure 12. Spatial distribution of horizontal differential stress in the shallow sediment layer (left) and accretionary prism layer (right). The magenta line indicates the trough axis. Triangles indicate the location of each observatory. The spatial interpolation method in 10 km circles around each observatory [*Smith and Wessel*, 1998] is used to obtain the spatial distribution of horizontal differential stress.

5 Discussion

For discussing the validity of horizontal differential stress estimated by our method, we used the stress polygon [e. g. *Chang et al.*, 2010] for both the shallow sediment layer and accretionary prism using P-wave velocity and density. The estimated horizontal differential stress in the shallow sediments and the accretionary prism beneath the C0002G observatory calculated in our method are shown in Figure 13. The vertical stress σ_v is given using the depth integration of the product of gravitational acceleration and density profile, which is calculated from P-wave velocity using Gardner's equation [*Gardner et al.*, 1974]. Internal frictions for calculating the stress polygon are 0.4 and 0.6 for shallow sediment layer and accretionary prism,

respectively, with reference to *Huffman et al.* [2016]. It is observed that the lines of the differential horizontal stress estimated from the S-wave anisotropy in the C0002G observatory reasonably pass inside the stress polygon calculated from the velocity model, although our method provides only the minimum values of the horizontal differential stress. We compared our results with existing results from borehole breakout analysis [*Kinoshita et al.*, 2009; *Chang et al.*, 2010; *Lin et al.* 2015; *Huffman et al.*, 2016] in the C0002 site, which is the only one site having resulted from plural methods. At this site, borehole breakout results indicated NE-SW orientations (41 ± 14°) for the azimuth of horizontal maximum stress, i.e., almost parallel to the trench axis at a depth of 200 to 1400 mbsf. The azimuth of the fast S-wave polarization obtained in the C0002 site respectively shows the azimuth of 60° in the shallow sediment layer and that of 144° in the accretionary prism layer. The results of S-wave anisotropy are consistent with the orientations of horizontal maximum stress inferred from borehole breakout analysis. The orientation of estimated horizontal maximum stress in the accretionary prism matches in the C0002 hole with the plate convergence direction, while that in the shallow sediment layer with the azimuth of the fast S-wave polarization estimated by multi-component data observed by OBS #74 located in the vicinity of the C0002 site at a distance of less than 1 km [*Tsuji et al.*, 2011a]. Results from the KMB07and KMD15 sites located along the seaward edge of the forearc basin showed a similar trend as that from the C0002 site, for which the azimuths of the fast S-wave polarization are ranging from 24 to 90° in the shallow sediment layer. These results are in good agreement with normal fault distribution estimated from a 3D seismic reflection survey [*Moore et al.*, 2013]. The agreement of results from the S-wave anisotropy with the others from the borehole breakout analyses and the interpretation of the seismic reflection survey implies that our approach could be used to estimate the azimuth of horizontal maximum stress and the horizontal differential stress as a function of space. Results may be discussed in terms of stress estimation around the Nankai seismogenic zone as follows:

-At landward observatories, KMA and KME obtained S-wave anisotropy, and estimated differential horizontal stress are relatively smaller than those in the offshore region, although there are some exceptions. The amplitudes of S-wave anisotropy are relatively weak, a maximum 4 %. The estimated differential horizontal stresses in the landward observatories are 0.2-1.1 MPa, and 1.6-4.1 MPa in the shallow sediment layer and accretionary prism, respectively. These results are reasonable compared to the horizontal differential stress of 2.7-5.5 MPa, estimated from P-wave anisotropy observed by the VSP survey conducted at the IODP C0009 borehole [*Tsuji et al.*, 2011] near the KME17 observatory. In the shallow sediment layer, at almost all observatories except KMA04, the orientations of the horizontal maximum stress are approximately perpendicular to the subduction direction. In the accretionary prism, the orientations of the horizontal maximum stress are almost parallel to the subduction direction. The results may suggest a subduction-parallel extensional field in the shallow sediment layer beneath the Kumano forearc basin, while a subduction-parallel compressional field in the accretionary prism layer, respectively. At the KMA04 site, the azimuth of the fast S-wave polarization in the shallow sediment layer appears parallel to the subduction direction, which is different from the other sites. Also, the magnitude of S-wave anisotropy at the KMA04 site is about 4.0 % [Table 2], which is relatively larger than those at the other sites. The site is located at the most landward side of the central part of the Kumano forearc basin, and the difference in the orientation and the magnitude of the S-wave anisotropy may be caused by the local structural three-dimensionality below the KMA04 site. Since the site is located close to the foot of the slope to the Kumano

basin, there may be a thin basin fill and shallow forearc substrata beneath the site. Since a few 3-D seismic images cover the area of the site [e.g., *Moore et al.*, 2013], future 3D seismic surveys are awaited to discuss the anomalous S-wave anisotropy observed at this site.

-The differential horizontal stresses are relatively strong, especially in the accretionary prism layer at the sites KMB07, KMD13, and KMD15 around the outer arc high of the southeast end of the Kumano forearc basin. The azimuths of the fast S-wave polarizations are parallel to the subduction direction in the accretionary prism, while orthogonal in the sediment layer inside the Kumano basin approximately orthogonal to the plate subducting direction. The minimum horizontal differential stresses are a few to several MPa in the accretionary prism layer. The azimuths of fast S-wave at the sites KMB07, KMD15, and C0002G inside the Kumano basin are all orthogonal to the subduction direction, and the minimum horizontal differential stresses are estimated about 0.9 – 1.5 MPa in the sediment layer, which might indicate that the uplifting of the outer arc high takes place due to the subduction to create a local tensile stress field inside the Kumano basin. In the C0002G borehole site, there is good agreement between the azimuth of the fast S-wave polarization and the horizontal maximum stress orientation inferred from borehole breakout analysis [*Kinoshita et al.*, 2009, *Chang et al.*, 2010, *Lin et al.*, 2015], which shows overall NE-SW directions (41 ± 14°).

-In the inner slope of the Nankai Trough, it is difficult to obtain stable results because of spatially-frequent topographic changes in the outer accretionary complex. The signal-to-noise ratio of the acquired seismic records was not high enough to identify reflected S-waves. Also, the Kuroshio, i.e., the westward intensified warm current in the Pacific, disturbed the position of the source vessel and caused hardship to adjust the vessel on the circle of the fixed radius of 3 km to each seismometer. At the site KMC09, only the deep reflection in the accretionary prism could be identified, while two reflection events from the shallow and from the deep could be estimated at the site KMC12. Obtained results show that the azimuths of the fast S-wave polarizations are approximately parallel to the subducting direction and are not changed with depth. The horizontal differential stresses are estimated to be 5.3-5.5 and 3.4 MPa at the sites KMC09 and KMC12, respectively, in the accretionary prism. In the shallow sediment layer at the site KMC12, the estimated horizontal differential stress was about 0.9 MPa, which may indicate the compressional stress due to the subduction would be effective in the deep close to the plate boundary while the relaxation of the stress takes place in the shallow inner slope due to the uplifting of outer arc high.

-We have conducted the circle shootings plural times at the seismometer locations and confirmed the repeatability of the survey to estimate the azimuth of the fast S-wave polarization and the magnitude of S-wave anisotropy within the range of 10° and 1.0%, respectively. The most considerable fluctuations observed in the repeated surveys at the sites KMA04 and KME17 were about 1.0%, which is about 0.8 MPa of the horizontal differential stress in the accretionary prism. The other sites showed less than 0.4% fluctuations in the magnitude of the S-wave anisotropy both in the shallow sediment layer and in the accretionary prism. The stress drop of megathrust earthquakes along the plate subduction zone is estimated as several MPa [e. g. *Seno et al.*, 2014]. When the stress drop and the interval of megathrust earthquakes at a location are

assumed to be respectively 3.0 MPa and 100 years, the average annual accumulation would be 0.03 MPa in the stress. Since the fluctuation of 0.4% of the magnitude of the S-wave anisotropy in the accretionary prism is about 0.3 MPa in the horizontal differential stress, i.e., ca. 10 times the annual accumulation of the megathrust earthquake, the variation of differential horizontal stress obtained might not be the change in the stress caused by the subduction, but would be the error in the measurements. Our method to estimate the horizontal differential stress has to be improved in accuracy as a measurement method of accumulating stress in the overhung. Since we know the positioning error of the seismic source along the circle survey line has a significant effect on the estimation of the peak in the anisotropy semblance, i.e., the final result of S-wave anisotropy, it is necessary to find a way to control the accuracy in the positioning of the source vessel.

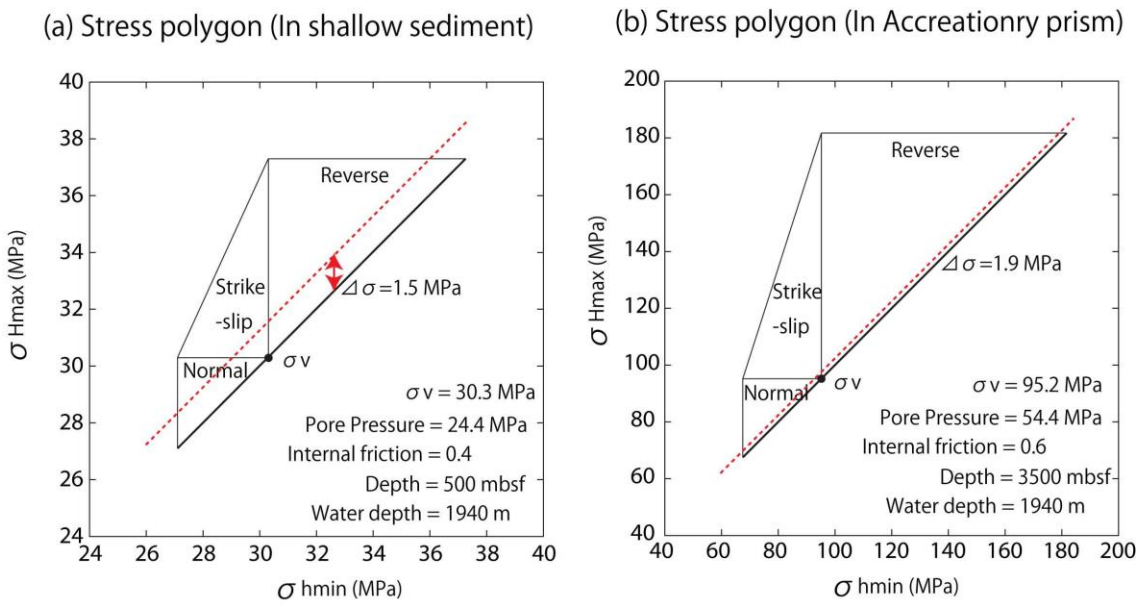

Figure 13. Comparison of calculated stress polygon and differential horizontal stress estimated from S-wave anisotropy (red dashed lines) in shallow sediment layer (a) and accretionary prism (b).

6 Conclusions

We performed a series of controlled-source seismic surveys around permanent seismic observatories to obtain S-wave anisotropy, the azimuth of the fast S-wave polarization, and the time difference of the fast and the slow S-wave arrivals in the Nankai Trough subduction zone. We applied a new technique called the "anisotropy semblance method" to obtain the depth-dependent S-wave anisotropy from the horizontal components of acquired seismic data for the shots of airguns along a circle of 3 km radius to each seismometer. We introduced a simple microcrack model to subseafloor materials to estimate the minimum values of differential horizontal stress from the obtained S-wave anisotropy parameters. Finally, we estimated the differential horizontal stress field around each observatory widely distributed in the Nankai Trough subduction zone and found good agreement between S-wave anisotropy and the horizontal differential stress obtained by the other methods. These results could be well

explained by tectonics of the Nankai Trough subducting zone. These results strongly suggested that the S-wave anisotropy below the seafloor in the Nankai Trough could be explained by the horizontal stress caused by the subduction. We think that the monitoring of the stress filed is possible through the observation of S-wave anisotropy. However, it is suggested that the positioning of the seismic source has to be improved when active sources are used to precisely estimate the stress accumulating in a time-lapse way.

Acknowledgments

We thank anonymous reviewers for helpful comments that significantly improved the manuscript. We also thank Dr. Weiren Lin and Dr. Hiroshi Asanuma for their helpful comments. DONET data used for this study were provided by the National Research Institute for Earth Science and Disaster Resilience (NIED). We used Generic Mapping Tools software [*Wessel and Smith*, 1998] and Seismic Unix [*Cohen and Stockwell*, 2011] to draw the figures. We thank the crews of R/V Kairei and the airgun operation team of the Nippon Marine Enterprises, Ltd. (NME) for acquiring high-quality data. The airgun shot time and location data observed during each cruise are available from the JAMSTEC database sites (KR13-17, https://doi.org/10.17596/0001201; KR15-05, https://doi.org/10.17596/0001221; KR15-08, https://doi.org/10.17596/0001224; KR16-11, https://doi.org/10.17596/0001246). The DONET seismometer data are available from the NIED database site (https://doi.org/10.17598/nied.0008). The borehole seismometer data are available from JAMSTEC database site (J-SEIS, https://join-web.jamstec.go.jp/join-portal/en/).

References

Alford, R. M. (1986), Shear data in the presence of azimuthal anisotropy, Dilley, Texas, 56th Annual International Meeting, *SEG, Expanded Abstracts*, 86, 81-82, doi: 10.1190/1.1893036.

Ando, M. (1975), Source mechanisms and tectonic significance of historical earthquakes along the Nankai Trough, Japan, *Tectonophysics*, 27,119–140, doi:10.1016/0040-1951(75)90102-X.

Araki, E., D. M. Saffer, A. J. Kopf, L. M. Wallace, T. Kimura, Y. Machida, et al. (2017), Recurring and triggered slow-slip events near the trench at the Nankai Trough subduction megathrust, *Science*, 356, 1157-1160, doi: 10.1126/science.aan3120.

Bale, R., T. Marchand, K. Wilkinson, K. Wikel and R. Kendall (2013), The Signature of Shear-Wave Splitting: Theory and Observations on Heavy Oil Data, *The Leading Edge*, 32, 14-24, doi: 10.1190/tle32010014.1.

Bansal, R. and M. K. Sen (2008), Finite-difference modelling of S-wave splitting in anisotropic media, *Geophys. Prospect.*, 56(3), 293-312, doi:10.1111/j.1365-2478.2007.00693.x.

Castagna, J. P., M. L. Batzle, and R. L. Eastwood (1985), Relationships between compressional-wave and shear-wave velocities in clastic silicate rocks, *Geophysics*, 50, 571–581, doi:10.1190/1.1441933.

615 Chang, C., L. C. McNeill, J. C. Moore, W. Lin, M. Conin, and Y. Yamada (2010), In situ stress
616 state in the Nankai accretionary wedge estimated from borehole wall failures, *Geochem.*
617 *Geophys. Geosys.*, 11, doi:10.1029/2010GC003261.

618 Cohen, J. K. and Jr. J. W. Stockwell (2011), CWP/SU: Seismic Unix Release No. 43: a free
619 package for seismic research and processing, Center for Wave Phenomena, Colorado
620 School of Mines.

621 Crampin, S. (1981), A review of wave motion in anisotropic and cracked elastic media, *Wave*
622 *Motion*, 3(4), 343–391, doi:10.1016/0165–2125(81)90026–3.

623 Crampin, S. and S. Chastin (2003), A review of shear wave splitting in the crack-critical crust,
624 *Geophys. J. Int.*, 155 (1), 221–240, doi: 10.1046/j.1365-246X.2003.02037.x.

625 Fujii, Y., K. Satake, S. Sakai, M. Shinohara and T. Kanazawa (2011), Tsunami source of the
626 2011 off the Pacific coast of Tohoku Earthquake, *Earth Planets Space*, 63,
627 doi:10.5047/eps.2011.06.010

628 Gao, Y. and S. Crampin (2004), Observations of stress relaxation before earthquakes, *Geophys.*
629 *J. Int.*, 157, 578-582, doi: 10.1111/j.1365-246X.2004.02207.x.

630 Gardner, G. H. F., L. W. Gardner and A. R. Gregory (1974), Formation velocity and density —
631 the diagnostic basics for stratigraphic traps, *Geophysics*. 39, p.770–780,
632 doi:10.1190/1.1440465.

633 Haacke, R. R., G. K. Westbrook and S. Peacock (2009), Layer stripping of shear-wave splitting
634 in marine PS waves, *Geophys. J. Int.*, 176, 782-804, doi:10.1111/j.1365-
635 246X.2008.04060.x.

636 Hirose, F., K. Kiyaoka, N. Hayashimoto, T. Yamazaki and M. Nakamura (2011), Outline of the
637 2011 off the Pacific coast of Tohoku Earthquake (Mw 9.0) —Seismicity: foreshocks,
638 mainshock, aftershocks, and induced activity—, *Earth Planets Space*, 63,
639 doi:10.5047/eps.2011.05.019.

640 Huffman, K. A., D. M. Saffer, and B. Dugan (2016), In situ stress magnitude and rock strength in
641 the Nankai accretionary complex: a novel approach using paired constraints from
642 downhole data in two wells, *Earth Planets Space,* 68, doi:10.1186/s40623-016-0491-4.

643 IMG FEAT/JAMSTEC (2016) Long-Term Borehole Monitoring System Continuous Data.
644 JAMSTEC, doi: 10.17596/0002136.

645 JAMSTEC (2014), KAIREI KR13-17 Cruise Data, JAMSTEC, doi: 10.17596/0001201.

646 JAMSTEC (2015a), KAIREI KR15-05 Cruise Data, JAMSTEC, doi: 10.17596/0001221.

647 JAMSTEC (2015b), KAIREI KR15-08 Cruise Data, JAMSTEC, doi: 10.17596/0001224.

648 JAMSTEC (2016), KAIREI KR16-11 Cruise Data, JAMSTEC, doi: 10.17596/0001246.

649 Kamei, R., G. Pratt, and T. Tsuji (2012), Waveform Tomography Imaging of a Megasplay Fault
650 System in the Seismogenic Nankai Subduction Zone, *Earth Planet. Sci. Lett.*, 317-318,
651 343-353, doi:10.1016/j.epsl.2011.10.042.

652 Kanamori, H. (1972), Tectonic implications of the 1944 Tonankai and the 1946 Nankaido
653 earthquakes, *Phys. Earth Planet. Inter.*, 5, 129–139, doi: 10.1016/0031-9201(72)90082-9.

Kawaguchi, K., S. Kaneko, T. Nishida and T. Komine (2015), Construction of the DONET real-time seafloor observatory for earthquakes and tsunami monitoring, in Favali, P. et al. (Eds.), *Seafloor Observatories* (pp. 211-228), Springer Praxis Books, doi 10.1007/978-3-642-11374-1_10.

Kimura, T., E. Araki, T. Takayama, K. Kitada, M. Kinoshita, Y. Namba, et al. (2013), Development and Performance Tests of a Sensor Suite for a Long-Term Borehole Monitoring System in Seafloor Settings in the Nankai Trough, Japan, *IEEE J. Oceanic Eng.*, 38, 383-395. doi: 10.1109/JOE.2012.2225293.

Kimura, T., H. Mikada, E. Araki, S. Kodaira and S. Miura (2016), Wide-area distribution of S-wave anisotropy estimated by airgun surveys around seafloor-cabled seismometers in the Nankai Trough, Japan, *SEG Technical Program Expanded Abstracts 2016*, 337-341, doi: 10.1190/segam2016-13972498.1.

Kinoshita, M., H. Tobin, J. Ashi, G. Kimura, S. Lallemant, E. J. Screaton et al. (2009), *Proc. IODP, 314/315/316: Washington, DC (Integrated Ocean Drilling Program Management International, Inc.)*, doi:10.2204/iodp.proc.314315316.200.

Kodaira, S., T. Hori, I. Aki, S. Miura, G. Fujie, J.-O. Park, T. Baba, H. Sakaguchi, and Y Kaneda (2006), A cause of rupture segmentation and synchronization in the Nankai trough revealed by seismic imaging and numerical simulation, J. Geophys. Res.,111, B09301, doi:10.1029/2005JB004030.

Kopf, A., E. Araki, and S. Toczko (2010), NanTroSEIZE Stage 2: riserless observatory, *IODP Sci. Prosp.*, 332, doi:10.2204/iodp.sp.332.2010.

Lin, W., M. L. Doan, J. C. Moore, L. McNeill, T. B. Byrne, T. Ito et al. (2010), Present-day principal horizontal stress orientations in the Kumano forearc basin of the southwest Japan subduction zone determined from IODP NanTroSEIZE drilling Site C0009, *Geophys. Res. Lett.*, 37(13), L13303, doi:10.1029/2010GL043158.

Lin, W., T. B. Byrne, M. Kinoshita, L. C. McNeill, C. Chang, J. C. Lewis et al. (2016), Distribution of stress state in the Nankai subduction zone, southwest Japan and a comparison with Japan Trench, *Tectonophysics*, 692, 120-130. doi:10.1016/j.tecto.2015.05.008.

Miyazaki, S. and K. Heki (2001), Crustal velocity field of southwest Japan: Subduction and arc-arc collision, *J. Geophys. Res.*, 106, 4305–4326. doi:10.1029/2000JB900312.

Moore G. F., B. B. Boston, A. F. Sacks and D. M. Saffer (2013), Analysis of normal fault populations in the Kumano Forearc Basin, Nankai Trough, Japan: 1 Multiple orientations and generations of faults from 3-D coherency mapping, *Geochem. Geophys. Geosys.*, 14, doi:10.1002/ggge.20119.

Nakano, M. and T. Tonegawa (2012), Orientations of DONET seismometers estimated from seismic waveforms, JASTEC Rep. Res Dev., 15, 77-89, doi: 10.5918/jamstecr.15.77 (in Japanese with English abstract).

National Research Institute for Earth Science and Disaster Resilience (2019), NIED DONET, National Research Institute for Earth Science and Disaster Resilience, https://doi.org/10.17598/nied.0003.

Nur, A. (1971), Effect of Stress on Velocity Anisotropy in Rocks with Cracks. *J. Geophys. Res.*, 76, 2022-2034. doi:10.1029/JB076i008p02022.

Okamoto, K., H. Mikada, T. Goto and J. Takekawa (2013), Utilization of Waveform for Estimating Stress Change in Time, *75th EAGE Conference & Exhibition incorporating SPE EUROPEC 2013*. doi: 10.3997/2214-4609.20131012.

Schubnel, A., P. M. Benson, B. D. Thompson, J. F. Hazzard, and R. P. Young (2006), Quantifying Damage, Saturation and Anisotropy in Cracked Rocks by Inverting Elastic Wave Velocities, *Pure Appl. Geophys.*, 163 (5-6), 947-973, doi:10.1007/3-7643-7712-7_3.

Seno, T., S. Stein and A. E. Gripp (1993), A model for the motion of the Philippine Sea plate consistent with NUVEL-1 and geological data, *J. Geophys. Res.*, 89, 17941-17948, doi: 10.1029/93JB00782.

Seno, T. (2014), Stress drop as a criterion to differentiate subduction zones where Mw 9 earthquakes can occur, *Tectonophysics*, 621, 198-210. doi:10.1016/j.tecto.2014.02.016.

Smith, W., P. Wessel (1990), Gridding with continuous curvature splines in tension, *Geophysics*, 55, 293-305, doi: 10.1190/1.1442837.

Suzuki, K., M. Nakano, N. Takahashi, T. Hori, S. Kamiya, E. Araki et al. (2016), Synchronous changes in the seismicity rate and ocean-bottom hydrostatic pressures along the Nankai trough: A possible slow slip event detected by the Dense Oceanfloor Network system for Earthquakes and Tsunamis (DONET), *Tectonophysics*, 680, 90-98, doi:10.1016/j.tecto.2016.05.012.

Thomsen, L., I. Tsvankin and M. C. Mueller (1999), Coarse-layer stripping of vertically variable azimuthal anisotropy from shear-wave data, *Geophysics*, 64, 1126-1138, doi:10.1190/1.1444619.

Tsuji, T., J. Dvorkin, G. Mavko, N. Nakata, T. Matsuoka, A. Nakanishi et al. (2011a), Vp/Vs ratio and shear-wave splitting in the Nankai Trough seismogenic zone: Insights into effective stress, pore pressure and sediment consolidation, *Geophysics* 76(3), WA71-WA82, doi:10.1190/1.3560018.

Tsuji, T., R. Hino, Y. Sanada, K. Yamamoto, J. O. Park, T. No et al. (2011b), In situ stress state from walkaround VSP anisotropy in the Kumano basin southeast of the Kii Peninsula, Japan, *Geochemistry Geophysics Geosystems*, 12, doi: 10.1029/2011GC003583.

Wallace, L. M., E. Araki, D. M. Saffer, X. Wang, A. Roesner, A. Kopf et al. (2016), Near-field observations of an offshore Mw 6.0 earthquake from an integrated seafloor and subseafloor monitoring network at the Nankai Trough, southwest Japan. *J. Geophys. Res. Solid Earth*, 121. doi:10.1002/2016JB013417.

Wessel, P., and W. H. F. Smith (1998), New, improved version of the generic mapping tools released, *Eos. Trans. AGU*, 79 (47), 579, doi: 10.1029/98EO00426.